Chapter 6
Magneto-Transport on Epitaxial Graphene

Peide D. Ye, Michael Capano, Tian Shen, Yanqing Wu, and Michael L. Bolen

6.1 Introduction

Graphene, a monolayer of carbon atoms tightly packed into a two-dimensional (2D) hexagonal lattice, has recently been successfully isolated from highly ordered pyrolytic graphite (HOPG) and shown to be thermodynamically stable and to exhibit astonishing transport properties, such as an electron mobility of $\sim$25,000 cm^2/Vs and velocity of $\sim 10^8$ cm/s at room temperature [1–3]. With the high carrier mobility enabled by its unique electronic structure, graphene has attracted many research efforts recently. Initial works have demonstrated the great potential of graphene for modern electronics applications. These efforts are focused on overcoming the challenges faced to incorporate graphene into microelectronic applications. The three particular challenges are developing a synthesis technique to manufacture graphene over wafer-scale areas, opening an energy bandgap in graphene, and forming a high-quality gate dielectric on the surface of graphene.

An interesting differentiation between the many well-established semiconductor materials in microelectronic industry and graphene is how it was discovered. Most semiconductor materials are created through deposition or melt processes, but the origin of graphene is unique. The first successfully isolated sheet of graphene was formed by Geim and Novoselov through a mechanical exfoliation technique which used cellophane tape to remove and subsequently transfer graphene sheets from HOPG to SiO_2 [2]. This produced graphitic flakes tens of microns in size upon which electronic devices were fabricated. The pioneering work on isolating graphene has been recognized by earning its discoverers the Nobel Prize in Physics for 2010. Since the mechanical exfoliation technique does not require expensive equipment, this approach is still widely used for research purposes. Various alternative methods have been studied and developed to fabricate uniform graphene

P.D. Ye (✉) · M. Capano · T. Shen · Y. Wu · M.L. Bolen
School of Electrical and Computer Engineering and Birck Nanotechnology Center, Purdue University, West Lafayette, IN 47907, USA

H. Raza (ed.), *Graphene Nanoelectronics*, NanoScience and Technology,
DOI 10.1007/978-3-642-22984-8_6, © Springer-Verlag Berlin Heidelberg 2012

on a large-scale with controlled layer thickness, including epitaxial graphene grown through the thermal decomposition of SiC [4–9] or chemical vapor deposition (CVD) growth of graphene on metallic substrates, such as copper or nickel [10–13], as described in Chap. 7.

Epitaxial graphene grown on the surface of SiC was first demonstrated three decades ago by Van Bommel [14] and developed further recently by de Heer and Berger et al. [4, 15]. This synthesis technique has proven to be one of the best available to produce high-quality, large-scale graphene. Compared to exfoliated graphene, epitaxial graphene formed by the thermal decomposition of SiC has provided the missing pathway to a viable electronics technology. The electronic band structure of graphene leads to a unique property which is its zero-bandgap. An energy bandgap is essential for typical digital applications as well as most RF applications. Many methods to engineer a bandgap within graphene have been studied such as tailoring nanoribbon structures [16–23] and using bilayer graphene with a displacement field [24–28]. Top gate configuration is a must for any device applications which require high-quality gate dielectric on graphene. Unlike silicon and other conventional semiconductor materials, the unique sp^2 hybridization of graphene provides no chemical bonds on the surface. This lack of bonds makes the surface chemically inert, which is problematic for forming high-quality dielectrics. There are many different solutions being investigated to solve this problem. One such approach is through the use of atomic layer deposition (ALD), the-state-of-the-art dielectric technique developed in Si CMOS technology [29, 30]. It has been found that a surface treatment of NO_2 gas can be used to functionalize the surface of graphene prior to the subsequent ALD of oxide [31]. Also, ultrathin seed layers such as an oxidized Al layer, a commercial NFC 1400–3CP (JSR Micro, Inc.), or perylene-3,4,9,10-tetracarboxylic dianhydride (PTCDA) polymer layers have been investigated [32–35]. Recently, a novel seed layer process using ozone and trimethylaluminum (TMA) as precursors at room temperature was also studied [36]. It is of great importance to provide a high-quality dielectric which does not degrade the channel mobility of graphene transistors. The dielectric should have high phonon energy and low interface trap density to minimize phonon scattering and impurity scattering.

In this chapter, the epitaxial graphene work on SiC performed at Purdue University in the past years is summarized. The summary includes the synthesis process, which uses an Epigress VP508 SiC hot-wall CVD reactor for graphene growth [5, 33, 37–40]. The physical characterization of the epitaxial graphene is discussed from systematic studies by scanning tunneling microscopy (STM), atomic force microscopy (AFM), transmission electron microscopy (TEM), and Raman spectroscopy. Furthermore, the ALD growth mechanism is investigated and ALD high-k/graphene integration is explored. Charge mobility is characterized by Hall mobility measurements and field-effect mobility characterization from top-gated devices. The authors have observed for the first time the half-integer quantum Hall-effect on epitaxial graphene which confirms that epitaxial graphene on SiC shares the same electrical properties as exfoliated graphene [33]. Similar findings were also reported by other groups independently [41–43]. Detailed magneto-transport studies

on monolayer graphene on SiC (0001) are also presented. Ballistic and coherent transport on nanostructured graphene films are also studied as well as spin transport. Related work has also been carried out at the George Institute of Technology, Naval Research Laboratory, Hughes Research Lab, IBM T.J. Watson Research Center, and many other universities.

6.2 Epitaxial Graphene Synthesis

The key to forming epitaxial graphene on SiC relies on controlling the preferential desorption of silicon atoms from the substrate. The first gas phase mass spectrometry studies of the thermal decomposition of SiC occurred in the late 1950s. It was shown that the most prevalent gaseous species sublimating from a thermally decomposing SiC substrate is atomic silicon [44, 45]. This desorption of silicon leaves behind a non-stoichiometric substrate in the form of a carbon rich surface as described in Chap. 5. After self-reconstruction and relaxation, the surface carbon minimizes its free energy through the formation of graphitic bonds. In situ studies using X-ray photoelectron spectroscopy (XPS) as well as Auger electron spectroscopy (AES) have demonstrated the formation of carbon-to-carbon sp^2 bonds [46]. These bonds form the hexagonal, or honeycomb-like, lattice characteristic of graphene. This graphitic film on SiC is generally referred to as epitaxial graphene.

By varying the thermal decomposition conditions, such as growth temperature, growth time, and chamber pressure, the material properties of the epitaxial graphene can be changed. As a simple example, increasing the growth time can increase the thickness of the epitaxial graphene. While true graphene is only a single monolayer thick, epitaxial graphene on SiC can possess the same electrical characteristics despite being multiple atomic layers thick. This is due to the symmetry and rotational stacking sequence of the individual layers within the epitaxial graphene [47]. Rotational stacking faults within epitaxial graphene serve to electronically decouple the individual layers and break the stacking symmetry of Bernal stacked graphite, which is the most common graphitic polytype. Depending on the polar face and growth conditions, uniform films with thicknesses of 1–2 layers or up to tens of layers can be reproducibly and reliably formed over the wafer scale.

The following is the developed process details used to grow high-quality graphene films on SiC. The epitaxial growth starts with a wet cleaning procedure using a Piranha bath and HF dip. Then the samples are transferred into an Epigress VP508 hot-wall CVD reactor for SiC surface preparation, and subsequently, graphene formation. The growth procedure is as follows:

1. A reactive hydrogen environment at 1,500°C is held for 10 min to remove polishing scratches.
2. The chamber is allowed to cool (typically to 700°C or below) while the hydrogen is evacuated.

3. The desired growth environment replaces the hydrogen, either high-vacuum or low-pressure Ar (1–100 mbar).
4. The chamber is brought to 1,100°C and then ramped at 10°C/min to the desired growth temperature (generally 1,350–1,650°C) for a desired length of time (generally 10 min).
5. Allow the chamber to cool naturally.

The growth conditions, film morphology, and electrical properties of the epitaxial graphene films differ markedly between films grown on the C-face (SiC $(000\bar{1})$) and films grown on the Si-face (SiC (0001)). This is because SiC is a polar material. It has been confirmed by several research groups that the graphene film is thicker for C-face grown graphene than Si-face under similar growth conditions [48]. For the C-face, there is only a single silicon-to-carbon sp^3 bond holding the desorbing silicon atom to the surface of the substrate, whereas for the Si-face, there are three bonds holding the silicon atom to the surface.

After growth and cooling, samples are taken out and inspected optically and with AFM. The AFM profilometry micrographs in Fig. 6.1 demonstrate how a growth condition, temperature in this case, affects the surface morphology. The hold time is kept constant at 10 min and a high-vacuum environment is used for this particular set of experiments. Comparing the micrographs, the most drastic change is seen between the 1,450°C and 1,500°C growth temperatures. At temperatures $\geq$ 1,500°C, several-micron large regions of smooth graphene films are obtained

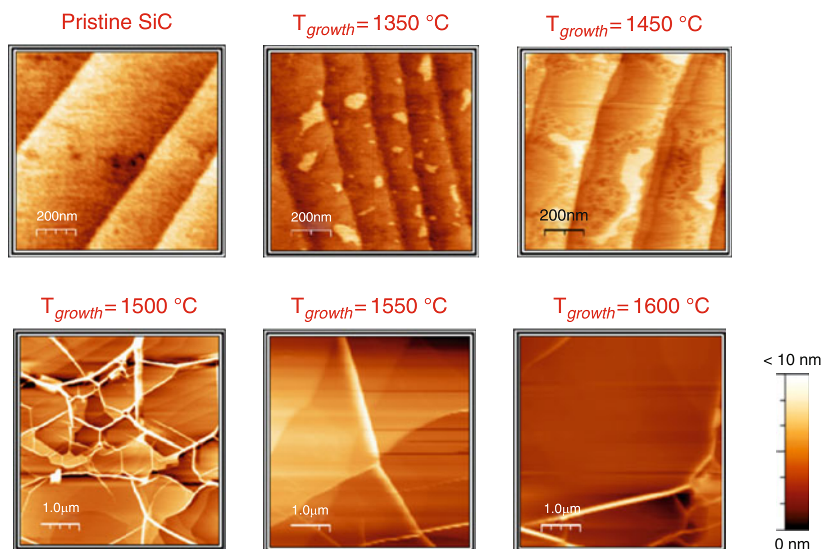

Fig. 6.1 AFM profilometry micrographs of C-face 4H–SiC substrates after H_2 etching and thermal decomposition at 1,350°C, 1,450°C, 1,500°C, 1,550°C, and 1,600°C for 10 min in vacuum (low-10^{-5} mbar). The images were taken by G. Prakash under the guidance of Prof. Reifenberger at Purdue University

which are delineated by ridges that are tens of nanometers high. As determined from angle-resolved XPS, the film itself grows linearly in thickness with increasing temperature. At 1,475°C, it is 1.7 nm thick and it is 5.7 nm thick at 1,600°C. Optimizing the growth conditions allows for thinner films. For example, gaseous argon can be used as a growth ambient as opposed to vacuum. At 1,600°C, using 10 mbar of argon overpressure instead of a vacuum environment is found to decrease the epitaxial graphene thickness by 1.1 nm. The argon overpressure creates an additional kinetic barrier to silicon desorption which can help control epitaxial graphene formation.

Unlike on the C-face, epitaxial graphene formation on the Si-face proceeds in a rate limited manner, which allows for synthesizing more uniform films. The morphology of epitaxial graphene film on the Si-face has a comparatively lower RMS roughness than the C-face due to a lack of ridges, as depicted in Fig. 6.2. Held at 1,550°C under vacuum for 10 min, the Si-face has epitaxial graphene covering approximately 95% of its surface. However, the typical Hall mobility of graphene formed on the Si-face under vacuum is ∼1,300 to 1,600 cm^2/Vs, which is significantly lower than the C-face samples grown at the exact same condition which exhibit a mobility value of ∼5,000 to 6,000 cm^2/Vs.

In addition to AFM, STM has also been used to study the surface of epitaxial graphene. An Omicron ultrahigh-vacuum STM with etched tungsten tips is operated at room temperature in the low 10^{-10} Torr regime. The XY piezocalibration was checked independently by imaging atoms in HOPG. Figure 6.3a shows a three-dimensional representation of epitaxial graphene blanketing the intrinsic terraces of

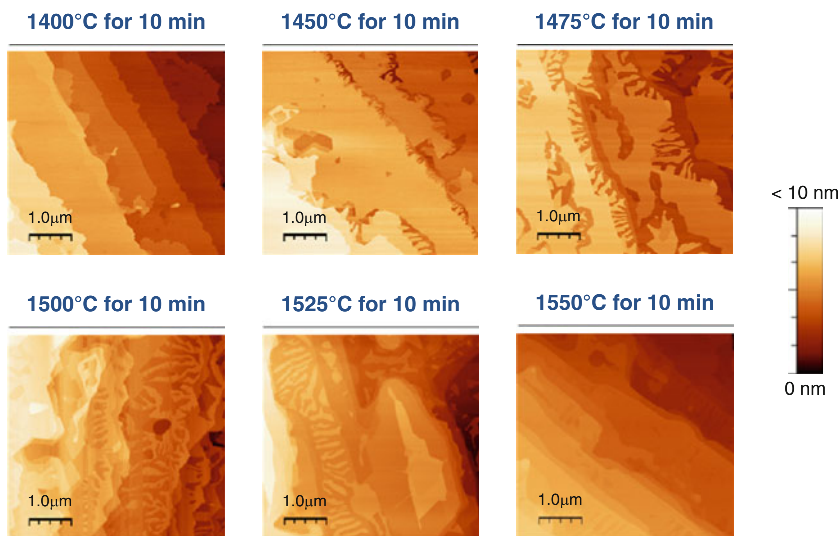

Fig. 6.2 AFM profilometry micrographs of Si-face SiC substrates after H_2 etching and thermal decomposition at 1,400°C, 1,450°C, 1,475°C, 1,500°C, 1,525°C, and 1,550°C for 10 min in vacuum (low-10^{-5} mbar)

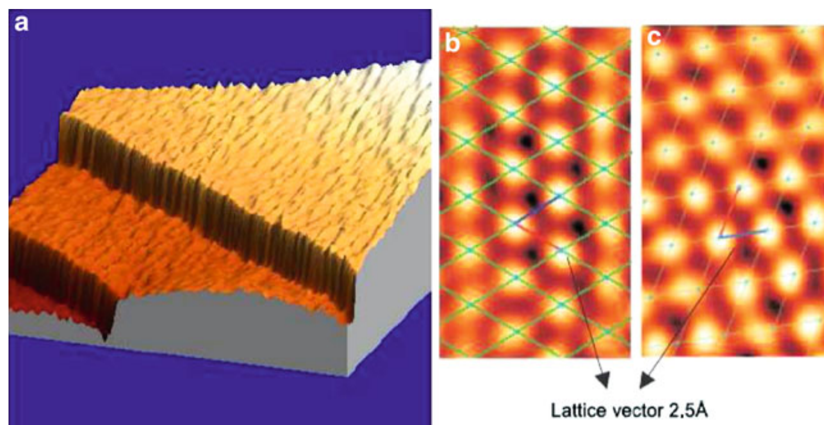

Fig. 6.3 (**a**) STM image of a graphene film formed on a carbon-face on-axis semi-insulating 4H–SiC substrate. The 1.2 or 1.4 nm steps are unit steps in the basal plane of the SiC substrate. (**b**) Atomic resolution STM image of a triangular sublattice of carbon atoms in a graphene film. Due to the offset between two sublattices in a multiple graphene film, only every other surface atom is imaged. The STM work was carried out by Prof. Reifenberger's group at Purdue University

the SiC surface. The local density of states (LDOS) are probed and exhibited in Fig. 6.3b. The measured lattice constant is found to be approximately 2.5 Å which is very close to that of graphene, which is 2.46 Å. Furthermore, the graphene on SiC has the same LDOS as on HOPG. Over atomistic length scales, this is material evidence of the high-quality graphene grown epitaxially on thermally decomposed SiC.

In addition to surface analysis, an atomistic side-view of epitaxial graphene can be obtained through the use of cross-sectional high-resolution TEM (HRTEM). This provides insight into the number of layers formed. Figure 6.4a shows a HRTEM micrograph of graphene layers formed on a Si-face sample held at 1,550°C for 10 min under high-vacuum. The sample is prepared for TEM via focused ion beam (FIB) extraction and then imaged at 300 kV with an FEI Titan 80–300. As can be seen, there is one monolayer of graphene plus a SiC reconstructed buffer layer between the graphene and SiC substrate. Throughout the tens of microns imaged from the extracted sample section, there are typically between 1–2 layers of graphene with a very few regions showing no signs of graphene. This lack of uniformity occurs since graphene formation relies on the pseudo-random process of Si desorption. Figure 6.4b shows another cross-sectional HRTEM image; this time of epitaxial graphene formed on the C-face after thermal decomposition at 1,500°C under vacuum. As previously mentioned, this thickness discrepancy between polar faces is common and thicker films are usually formed on the C-face of SiC under similar growth conditions.

Hall bars are fabricated on epitaxial graphene on both polar faces to understand the quality of the film over a larger length scale than the atomistic views provided by HRTEM and STM. The measured Hall mobility values for both C-face and Si-face devices are presented in Fig. 6.5. The positive correlation between growth pressure

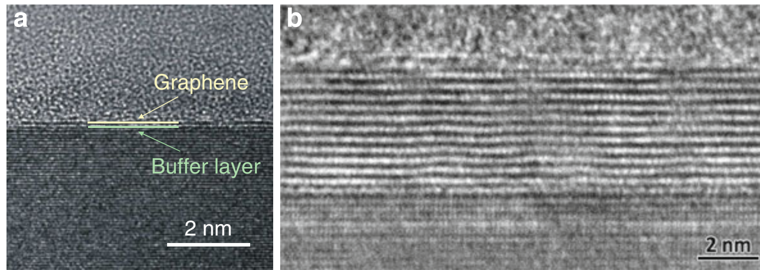

Fig. 6.4 HRTEM micrographs of (**a**) Si-face and (**b**) C-face SiC substrates after 1,550°C and 1,500°C thermal decomposition for 10 min, respectively. The FIB and TEM work was performed by R. Colby under the guidance of Prof. Stach at Purdue University

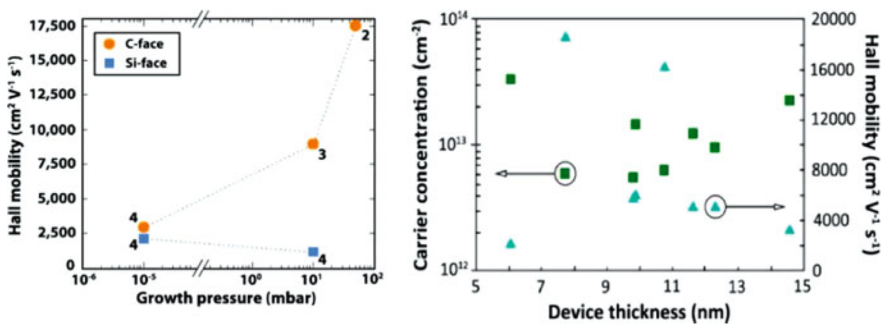

Fig. 6.5 (**a**) Average room-temperature Hall mobility values versus pressure for both C-face and Si-face devices. The graphene coverage is discontinuous at chamber pressures above 50 mbar for the C-face and 10 mbar for the Si-face. The number next to each point represents the number of devices tested, and the *dotted lines* serve as guides to the eye. (**b**) There is no apparent correlation between the thickness of a Hall bar and its measured Hall mobility or carrier concentration. This implies that there is not equal conduction from each graphene layer in the film

and mobility for the C-face is similar to that found by Tedesco et al. [48]. This correlation continues to the point where a large enough Ar overpressure inhibits Si desorption from the SiC sample and epitaxial graphene formation is halted. At 100 mbar (50 mbar) and 10 min growth time, AFM and Raman spectroscopy indicate there is no longer a continuous film of epitaxial graphene on the C-face (Si-face) surface. Instead, on the C-face, isolated patches of epitaxial graphene are found at random locations across the surface. With increased growth time, it is expected, based on previous research, that a continuous film would be achieved at 100 mbar; but for this set of experiments, growth time is held constant at 10 min. There is not a clear increase in Hall mobility values as pressure increases on the Si-face, unlike the trend other groups have observed [49, 50]. This discrepancy could be caused by an increasing density of discontinuities in the epitaxial graphene. As growth pressure increases, so too does the suppression of Si desorption, which leads to a discontinuous epitaxial graphene film. Thus, there is a decrease in the percentage of the surface which is covered by epitaxial graphene as growth pressure increases.

This notion is confirmed via AFM phase contrast imaging. These discontinuities serve as scattering sites, thereby lowering the overall measured Hall mobility.

Figure 6.5b shows an apparent lack of correlation between the thickness of each device and its Hall mobility and carrier concentration value. This is important, because it implies that each graphene layer within the epitaxial graphene does not contribute equally to conduction. If there were equal conduction, then for each additional layer, there would be a monotonic increase in carrier concentration with thickness. Correspondingly, there would be a decrease in the Hall mobility value, since carrier concentration and Hall mobility are inversely related. Instead, neither of these trends are apparent in Fig. 6.5b.

6.3 Dielectric Integration on Epitaxial Graphene

ALD is a thin-film growth technique for depositing uniform and conformal films with atomic precision. ALD is a special modification of the CVD method with the distinctive feature of alternate and cyclic supply of each gaseous precursor to the reactor chamber at relatively low temperature 200–350°C. The alternating pulses of the precursors are chemisorbed on the substrate surface and excesses are removed by a purge step. The key feature of the ALD methods is the saturation of all the reaction and purging steps, which makes film growth self-limiting on the surface. The precision achieved with ALD allows processing of nanometer-scale films in a controlled manner. ALD methods and applications have developed rapidly over the last ten years, particularly for high-k gate oxides. ALD high-k Hf-based oxide has become a manufacturing process to replace SiO_2 in 45 nm node Si complementary metal-oxide semiconductor (CMOS) digital integrated circuits starting in the second half of 2007. It is natural to extend this state-of-the-art CMOS oxide processing technology to graphene. However, the ALD process on graphene is expected to be very different from the deposition on conventional semiconductors or oxides, because the perfect graphene surface is chemically inert [51].

Figure 6.6a shows an AFM topography image of fresh HOPG surface with an atomically smooth (rms $= 0.04$ nm) carbon surface and atomically sharp step edges created by broken graphene layers. From the line profile (not shown), the step height is measured to be 0.3–0.4 nm, confirming that it is generated by a single graphene layer. Figure 6.6b shows an AFM image of a similar area after 10 cycles, i.e., 1 nm of ALD Al_2O_3 process at 250°C growth temperature. From these images and line profile data (not shown), the graphene surface remains atomically smooth with an rms roughness of 0.04 nm, indicating that no Al_2O_3 films are grown on graphene surface. This demonstrates that conventional H_2O-based ALD process cannot grow two-dimensional, continuous, and isotropic oxide films directly on pristine graphene surfaces. On the other hand, Al_2O_3 nanoribbons with 1.5 nm height and several nanometers wide are clearly observed at step edges, indicating that ALD Al_2O_3 films only grow along the step edges.

It is widely believed that an ultrathin high-k dielectric integration on graphene would be the next major road block toward the realization of high-performance

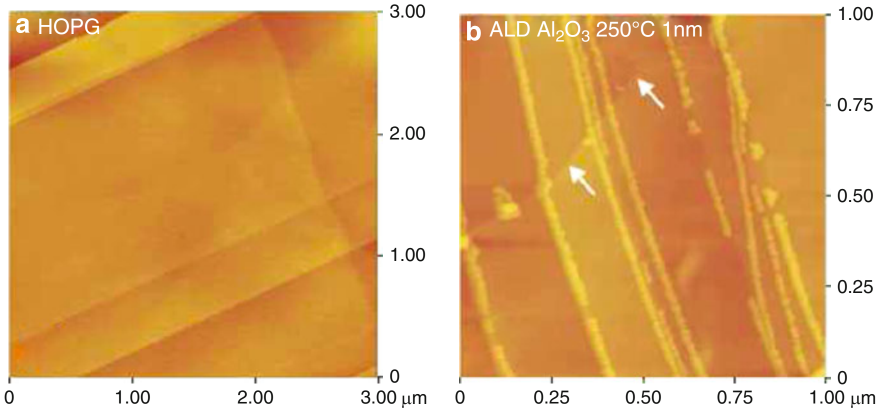

Fig. 6.6 (**a**) AFM images of HOPG surface with graphene terraces and (**b**) similar surface after 1 nm thick ALD Al_2O_3 growth

graphene-based electronic devices. Much research has been carried out in this field using specific seeding or interfacial layers, as has been done with Ge or III–V semiconductors. These research efforts can be categorized as: (1) trimethylaluminum (TMA) + NO_2 seeding layer [31, 51], (2) TMA + O_3 seeding layer [36], (3) a fully oxidized Al seeding layer [32, 33], (4) organic PTCA or PTCDA seeding layer [30,35], and (5) diluted spin-coated polymer NFC 1400–3CP as a buffered dielectric [34]. Significant additional research is needed to characterize the interface quality and optimize the dielectric formation process at the device level. Our approach is to form ALD high-k gate stack integration on epitaxial graphene films by inserting a 1 nm thick fully oxidized Al film as a seeding layer. The gate stack formation does not degrade the electrical properties of epitaxial graphene films significantly. The half-integer quantum Hall-effect (QHE) is observed in gated epitaxial graphene films on SiC (0001), along with pronounced Shubnikov-de Haas (SdH) oscillations in magneto-transport [33]. The observation of quantum features demonstrates the reasonable success of integration of ALD high-k on epitaxial graphene.

6.4 Top-Gate Graphene Field-Effect Transistors

For most potential graphene applications, it is crucial to have a top gated working transistor that can be integrated into a conventional CMOS process flow, and that enables device scaling. Conventional transistors are made on semiconductors with moderate bandgap (Si $\sim$ 1.12 eV, GaAs $\sim$ 1.4 eV). Bandgap is an important characteristic of the semiconductor that enables the device to turn off and minimizes leakage current at off state. The bandgap energy also influences two performance parameters that tend to offset one another: drive current (mobility) and on–off ratio.

Generally, for narrow bandgap semiconductors, the light effective mass enables high mobility and even ballistic transport. However, in narrow bandgap semiconductors, the off current becomes excessive because band-to-band tunneling current is large. Graphene has very high mobility and room temperature ballistic transport over a few hundred nanometers, which is one of its most attractive properties for device performance. The biggest concern currently for graphene is the poor off-state characteristics. Narrow ribbon widths down to less than 10 nm are required to induce a bandgap and achieve acceptably low off currents. Narrow ribbons of these dimensions are still a challenge, even with modern lithographic techniques [16,17]. The edge roughness of the nanoribbon at 10 nm scale leads to the significant degradation of the intrinsic mobility. Graphene edge surface passivation is another active field currently [52–54].

Because the density of states (DOS) in graphene is linear with respect to the energy level, gate voltage can modulate the DOS linearly to enable modulation of current in the channel. Top-gated transistors have been fabricated and characterized on epitaxial graphene on SiC on both (0001) and $(000\bar{1})$ face of SiC [5]. The device structure of the fabricated graphene FET is shown in Fig. 6.7a. Device isolation of the graphene film was realized by 120 nm deep SF_6-based dry etching with photolithographically defined photoresist as a protection layer. Ti/Au metallization was used to form Ohmic contacts on graphene as source and drain. Physical vapor deposited (PVD) SiO_2 was used as a top gate dielectric. Finally, conventional Ni/Au metals were electron-beam evaporated, followed by lift off to form the gate electrodes. The process requires three levels of lithography (isolation, Ohmic, and gate), all done using a contact mask aligner. PVD dielectrics can be simply applied to graphene devices instead of ALD. However, it is also a challenge to form nanometer thin high-quality dielectric on graphene by the PVD approach.

Figure 6.7a shows the DC output characteristic with a gate bias from 1 to 2.5 V on a device with a fully covered gate. The measured graphene FET has a designed gate length (L_g) of 400 μm and a gate width (L_w) of 50 μm, with a gate oxide of 50 nm SiO_2. The gate leakage current is very low, below 10^{-9} A under the same bias conditions, corresponding to a gate leakage current density of 3×10^{-6} A/cm^2. The drain current can be modulated by approximately 50% with gate bias of a few volts. A reference SiC sample without the graphitization treatment, processed at the same time, shows no current (<40 pA), which confirms conduction through the graphene layers only. Figure 6.7b illustrates the transfer characteristics of this graphene FET at $V_{ds} = 2.0$ V. The drain current or conductance exhibits a region of minimum at $V_{gs} \approx -0.8$ V. This dip in single-graphene layer is well-documented and corresponds to a minimum conductivity of $\sim 4e^2/h$ at the charge neutrality point or Dirac point, where e and h are the electric charge and Planck's constant, respectively. It is the same physical origin here for multilayer graphene films. The device cannot be turned off because graphene or graphite is a semimetal with no bandgap. A finite bandgap can be created by patterning graphene into graphene nanoribbons, but the dimensions of such ribbons press the limits of modern lithography. The slope of the drain current shows that the peak extrinsic transconductance (G_m) is $\sim$1.4 mS/mm, due to its extraordinarily large gate length.

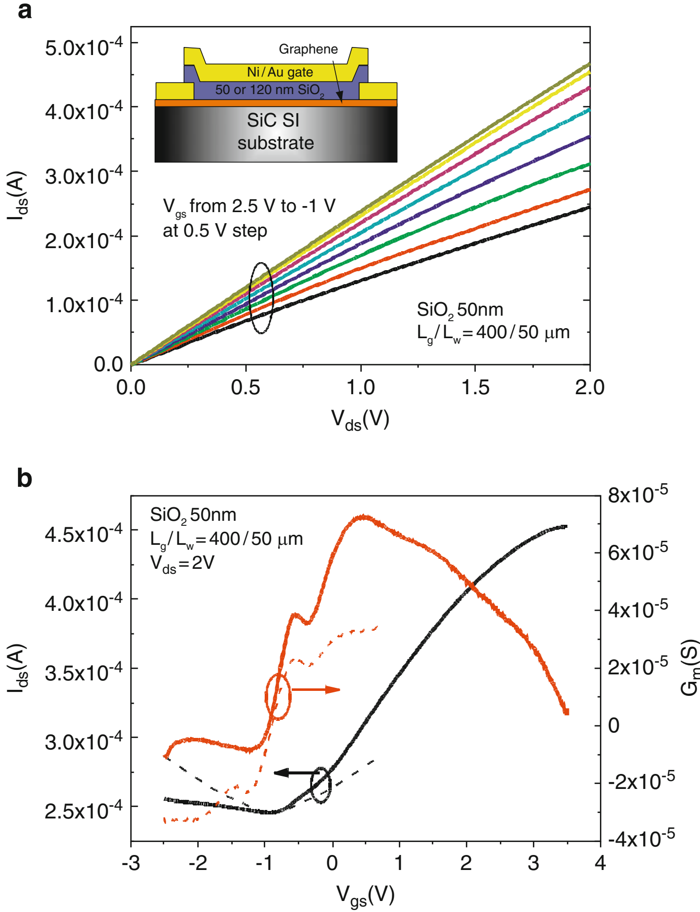

Fig. 6.7 (**a**) I_{ds} vs. V_{ds} as a function of V_{gs} on a few-layer graphene FET measured at room temperature. V_{gs} changes from 2.5 V (*top*) to 1.0 V (*bottom*) in 0.5 V steps. *Inset*: device structure of the top-gate transistor on epitaxial graphene on SiC substrate. (**b**) Transfer characteristics of the same device at $V_{\mathrm{ds}} = 2$ V. The *dashed lines* are corrected one around Dirac point after extracting the p–n junction resistance or odd resistance component

The channel mobility can be simply estimated by:

$$\mu = \left[\left(\Delta I_{\mathrm{d}} / V_{\mathrm{ds}} \right) / \left(L_{\mathrm{w}} / L_{\mathrm{g}} \right) \right] / C_{\mathrm{ox}} \Delta V_{\mathrm{gs}} \tag{6.1}$$

using the surface-channel device formula. Here, C_{ox} is determined by $\varepsilon_0 \varepsilon_{\mathrm{r}} A/d$, where ε_0 is the permittivity of free space, ε_{r} is 3.0 for PVD SiO_2 without annealing, A is the cross-sectional area, and d is the gate oxide thickness. The extracted electron effective mobility is as high as $5,400\,\mathrm{cm}^2/\mathrm{Vs}$. The device characteristics become ambipolar for low charge density near the Dirac point. A simple approach,

proposed by Huard et al., is used to further characterize the sample by extracting the p–n junction resistance [55], as shown by the dashed lines in Fig. 6.7b. The corrected electron mobility drops from 10% to 30% around Dirac point at $V_{gs} = -0.8$ V. Note that this correction is not necessary under unipolar conditions or at high charge density.

6.5 Half-Integer Quantum Hall-Effect in Epitaxial Graphene

Recent reports of large-area epitaxial graphene by thermal decomposition of SiC wafers have provided the missing pathway to a viable electronics technology [4–9]. An interesting question that remains to be addressed is whether the electrical properties of epitaxial graphene on SiC are similar to those in exfoliated graphene films [1–3]. For example, the well-known quantum Hall-effect (QHE), a distinguishing feature or hallmark of a 2D electronic material system, has been observed only very recently in epitaxial graphene on both the Si-face [33, 41, 42] and the C-face [43] of SiC. This question is discussed in this section.

Graphene layers on the Si-face of SiC, with a one-nanometer fully oxidized Al seeding layer grown by ALD to form an Al_2O_3 gate dielectric, were used to examine transport properties. The graphene growth temperature and time were 1,600°C for 10 min in a vacuum of 10^{-5} mbar. Standard Hall-bar devices for magneto-transport measurements were fabricated. Four-point magneto-transport measurements were performed in a variable temperature (0.4 K to 70 K) ^{3}He cryostat in magnetic fields up to 18 T using standard low frequency lock-in techniques. The external magnetic field (B) was applied normal to the graphene plane. Figure 6.8a shows the magneto-resistance R_{xx} and the Hall resistance R_{xy} as a function of magnetic field B from -18 T to 18 T at 0.8 K. From the Hall slope, the electron density is determined to be $1.04 \times 10^{12}/\text{cm}^2$ and Hall mobility of 3,580 cm^2/Vs at 0.8 K. No significant mobility degradation is observed after ALD gate dielectric. At high magnetic fields, R_{xy} exhibits a plateau while R_{xx} is vanishing, which is the fingerprint of the QHE and SdH oscillations. One well-defined plateau with value $(h/2e^2)$ is observed at $|B| > 15.5$ T, while two higher-order plateaus are developing with values of $(h/6e^2)$ and $(h/10e^2)$, respectively. The pronounced SdH oscillations with at least four distinguishable peaks are also observed at the corresponding magnetic fields. The precision of the plateau is better than 1 part in 10^4 within the instrumental uncertainty. It shows the QHE in epitaxial graphene is also applicable for metrology applications. The R_{xy} quantization in this epitaxial graphene film is in accordance with $[h/(4n+2)e^2]$, where n is the Landau level index, found in exfoliated graphene as a distinguishing feature of Dirac electrons. It is significantly different from conventional Fermi electrons with plateaus of (h/ne^2). The observed well-defined half-integer QHE reproduces the unique features observed in exfoliated single-layer graphene including a Berry phase of π. The observed QHE on this epitaxial graphene confirms that epitaxial graphene on SiC (0001) and exfoliated single-layer

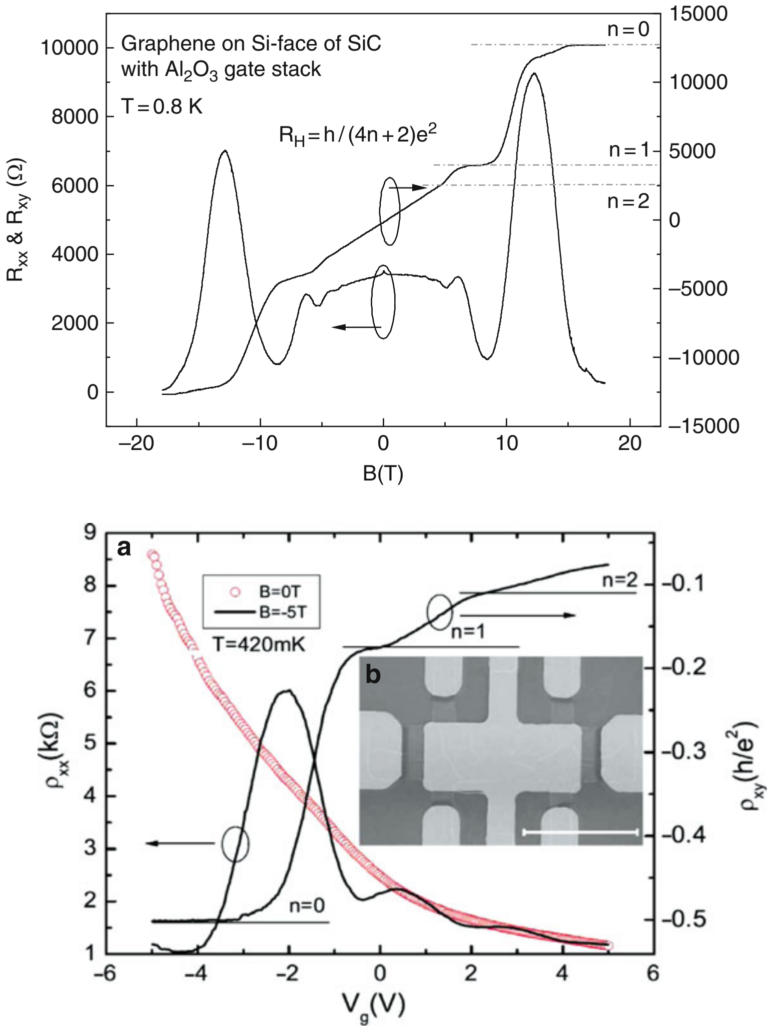

Fig. 6.8 (**a**) Hall resistance and magneto-resistance measured in the device at $T = 0.8$ K and with floating gate bias. The *horizontal dashed lines* corresponding to $h/(4n + 2)e^2$ values. The QHE of the electron gas in epitaxial graphene is shown one quantized plateau and two developing plateau in R_{xy}, with vanishing R_{xx} in the corresponding magnetic field regime. (**b**) Four-terminal resistance as a function of top gate bias (V_g) of the device, grown at 1,600°C in vacuum on SiC (0001), measured at 420 mK with zero magnetic field (*open circles*) and -5 T (*solid lines*). *Inset*: SEM image of a fabricated device. The scale bar is 20 μm

graphene are governed by the same relativistic physics with Dirac particles as transport carries [1–3].

Similar four terminal longitudinal resistivity ρ_{xx} and Hall resistivity ρ_{xy} can also be measured at a constant high magnetic field by changing the carrier density.

Figure 6.8b shows the magneto-transport measurement for a similar device at 420 mK, where the top gate is varied between −5 V and 5 V. At zero magnetic field, ρ_{xx} drops from ∼8.6 kΩ to ∼1.2 kΩ, with an on–off ratio of ∼7. The increase of ρ_{xx} with the decrease of V_g confirms the initial n-type doping of the graphene channel. So far, in this bias range, the Fermi level cannot sweep through the charge neutrality point, due to the heavy doping during the initial graphene growth. At −5 T, most remarkably, ρ_{xy} exhibits clearly quantized plateaus at $h/2e^2$, $h/6e^2$ for electrons accompanied with the minimum in ρ_{xx}, and the higher order plateaus are developing. It leads to the same conclusion as described above that monolayer graphene can be formed on SiC (0001) surface and its electrical property is the same as the exfoliated single-layer graphene governed by the relativistic physics with Dirac fermions as transport carriers.

Applying negative bias can dramatically decrease the carrier density, and makes the low filling factor QHE more easily visible. This approach is exploited by biasing the device at −5 V, which corresponds to an electron density of $2.2 \times 10^{11}/\mathrm{cm}^2$ and mobility of $3,250\,\mathrm{cm}^2/\mathrm{Vs}$ at 420 mK, and measuring the temperature dependence of ρ_{xx} and ρ_{xy} as shown in Fig. 6.9. Note that ρ_{xx} does not fully vanish at high magnetic field even at the lowest temperature. We ascribe this observation to the defect induced scattering that broadens the Landau level and the relatively large contact resistance, which is more than 10 kΩ μm caused by the fabrication process. Nevertheless, the $n = 0$ quantum Hall plateau and the corresponding SdH minimum are still pronounced, even at temperatures as high as 70 K, reaching the liquid nitrogen temperature. More efforts on measuring the same device at room temperature (not shown) reveal the modulation in ρ_{xx} and saturation in ρ_{xy} at 18 T. We believe with further engineering on the device fabrication as well as graphene film growth, it is very possible to observe the $n = 0$ quantum Hall plateau at room temperature and reasonable magnetic field. Room temperature QHE on

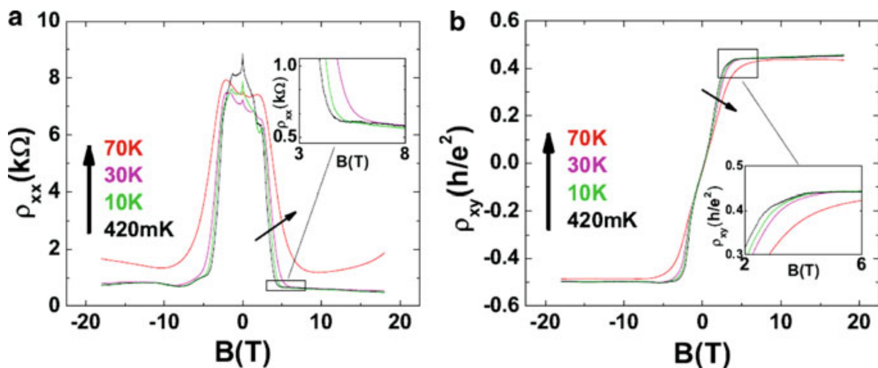

Fig. 6.9 Temperature dependence of ρ_{xx} and ρ_{xy} at $V_g = -5$ V. (**a**) Pronounced SdH minimum remain up to 70 K. (**b**) Pronounced $n = 0$ quantum Hall plateau remains up to 70 K. It is expected to remain up to room temperature

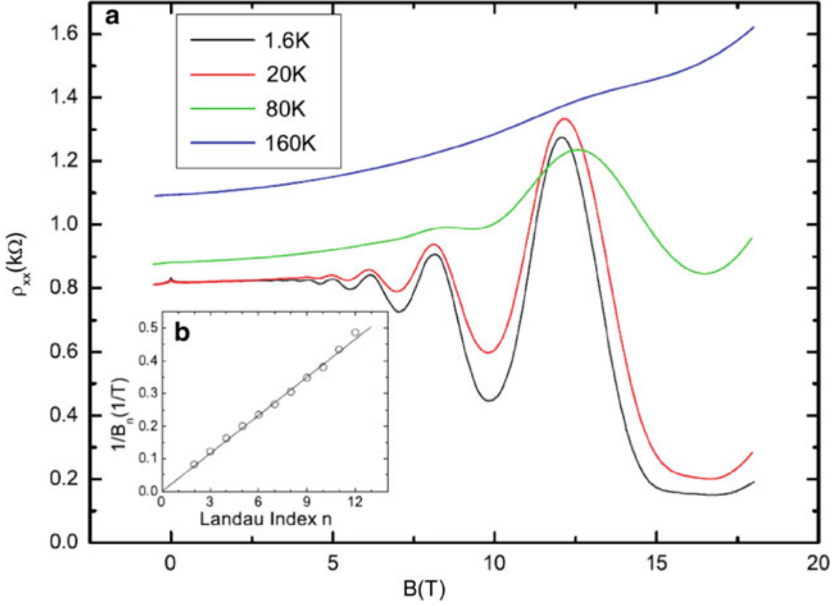

Fig. 6.10 (**a**) Temperature dependence of ρ_{xx} for a device, grown at 1,600°C and 10 mbar argon ambient, at $V_g = 1.8$ V from 1.6 K to 160 K. (**b**) Landau plot of the maximum of the SdH oscillations up to 18 T at 1.6 K. n is the Landau index and B_n is the magnetic field at the corresponding maxima of the oscillations. The *circles* are the experimental data and the *solid line* is the linear fitting. The zero y intercept indicates the Berry's phase of π [3]

epitaxial graphene could be an interesting topic as a quantum resistance standard for metrology applications [42].

To further understand the underlying physics, Landau plot, e.g., the Landau index vs. the inverse of the magnetic field, is investigated as shown in Fig. 6.10b. Here, we start with a sample grown at 1,600°C in a 10 mbar argon ambient, which has a much higher electron density, while more suitable for this purpose due to its more pronounced SdH oscillation peaks, as shown in Fig. 6.10a. The Landau index data are taken at the maximum of the SdH oscillations up to 18 T at 1.6 K. The open circles are the experimental data and the solid line is the linear fitting. The zero y intercept indicates the Berry's phase of π, the hallmark feature for monolayer graphene in electrical transport. From the slope, we can find the carrier density to be $2.46 \times 10^{12}/\mathrm{cm}^2$, consistent with $2.37 \times 10^{12}/\mathrm{cm}^2$ deduced from the Hall slope.

The damping of the SdH oscillations in Fig. 6.10a is caused by thermal broadening of Landau levels. The temperature dependence of the relative peak amplitudes in graphene is given by [56]:

$$A_n(T)/A_n(0) = t_k/\sin ht_k, \tag{6.2}$$

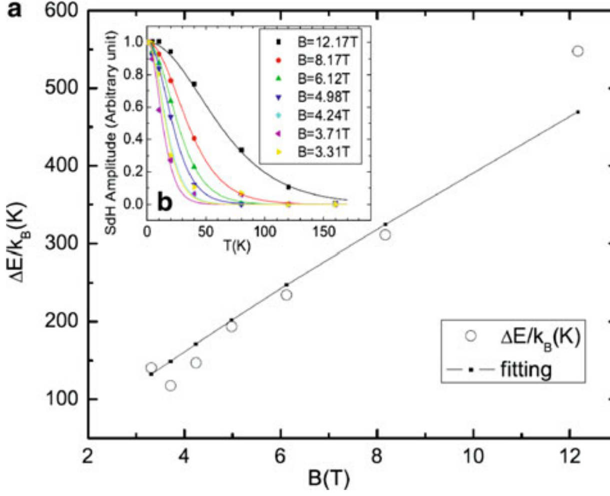

Fig. 6.11 (**a**) Fitting to the Fermi velocity v_F according to the Landau level separation. (**b**) Relative SdH peak fitting according to (6.1) for different temperatures at each peak

where $A_n(T)$ is the relative peak amplitude of the nth SdH peak at temperature T, and $t_k = 2\pi^2 k_B T/\Delta E(B)$ with:

$$\Delta E(B) = E_{n+1}(B) - E_n(B) \tag{6.3}$$

$$= \left(\sqrt{n+1} - \sqrt{n}\right) v_F \sqrt{2eB\hbar} \tag{6.4}$$

the Landau level separation (Fig. 6.11). The experimental value of Landau level separation is determined by fitting the relative SdH peaks according to (6.2) for different temperatures at each peak, as shown in Fig. 6.10b. The relative amplitude is normalized for each peak, for better viewing. The corresponding $\Delta E(B)$ is plotted versus B as the open circles in Fig. 6.10a. The dotted line is the fitting of $\Delta E(B)$ versus B according to (6.4). The fitted v_F is 1.01×10^8 cm/s. Similar analysis were carried out for two other devices grown at 1,600°C SiC (0001) in vacuum, with $v_F = 1.05 \times 10^8$ cm/s and 9.94×10^7 cm/s, respectively. The fitted Fermi velocity agrees remarkably well with the accepted value of $v_F = 1.00 \times 10^8$ cm/s for graphene.

In the center of the impurity broadened Landau level, the localization length ξ, i.e., the spatial extension of the electron wave function, diverges as a power law $\xi \approx (E - E_c)^{-v}$ with a universal critical exponent v [57], where E_c is the energy of a Landau level center. Since E_c varies as the B varies, the derivatives $(d\rho_{xy}/dB)^{max}$ between the plateau to plateau transition, and the half-width in ρ_{xx} which is defined as the distance ΔB between the two extreme in $d\rho_{xy}/dB$, provide the experimental measure of the delocalization phenomenon in the integer quantum Hall regime [57]. It has been found that, below a certain characteristic temperature T_{sc}, $(d\rho_{xy}/dB)^{max} \approx T^{-\kappa}$ and $\Delta B \approx T^{\kappa}$, where $\kappa \approx 0.42$ is

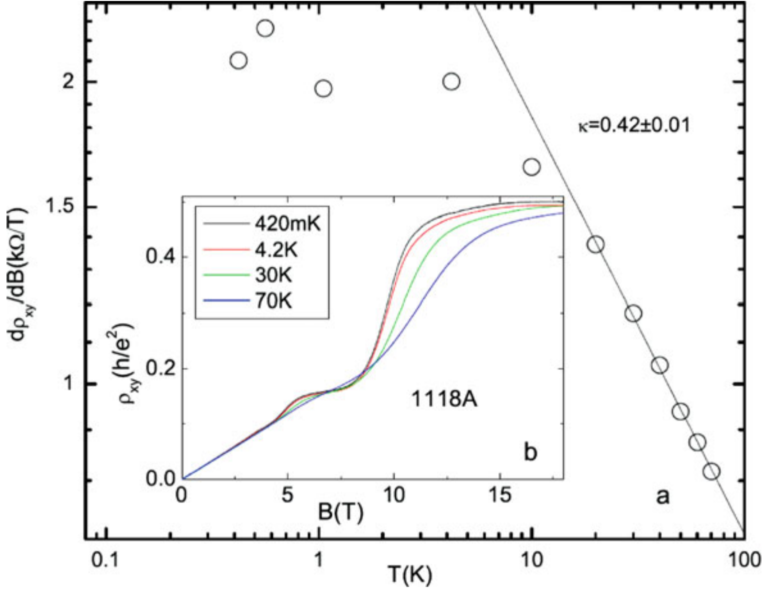

Fig. 6.12 The derivative $(\mathrm{d}\rho_{xy}/\mathrm{d}B)^{max}$ as a function of temperature for the $n = 1$ plateau to $n = 0$ plateau transition of sample 1,118 A. The *open circles* are the experiment data and the *solid line* is the fitting for the highest 6 temperature points. (**b**) ρ_{xy} of sample 1,118 A from 420 mK to 70 K at $V_g = 0$ V

universal for conventional 2D systems [57–59], and exfoliated graphene [60]. Here, we demonstrate that the universal scaling behavior also holds for epitaxial graphene. Compared to the other conventional 2D systems, graphene T_{sc} is much high than the very low temperature (mK), thus allowing us to probe the same physics at temperatures higher than liquid helium temperature.

Figure 6.12 shows the temperature dependent quantum Hall-effect from 420 mK to 70 K at $V_g = 0$ V for a sample grown at 1,600°C on the Si-face of SiC. Since this specific sample shows the best plateau to plateau transition, it is a good starting point to analyze the scaling behavior. Figure 6.12 shows the temperature dependent derivative $(\mathrm{d}\rho_{xy}/\mathrm{d}B)^{max}$ for the $n = 1$ plateau to $n = 0$ plateau transition of the same sample. The open circles are the experiment data and the solid line is the fitting for the highest 6 temperature points. As the temperature drops down, $(\mathrm{d}\rho_{xy}/\mathrm{d}B)^{max}$ starts to saturate, showing that ξ is not dominated by temperature, but rather by an intrinsic length scale, possibly equivalent to the sample size [57–59]. The slope shows $\kappa = 0.42 \pm 0.01$ agrees remarkably well with the accepted universal value of 0.42. We did detailed studies on two devices with B sweeps and another two devices with gate bias sweeps. All four devices show the near universal value of 0.42 on the filling factor 2 to 6 transitions.

6.6 Ballistic and Coherent Transport on Epitaxial Graphene

Antidot arrays are interesting structures to study because of their transport properties in conducting electronic materials. Antidots can be regarded as groups of imposed scattering centers that limit the ballistic transport or the mean free path of carriers [61]. Antidot arrays can also be considered as an ensemble of Aharonov–Bohm (AB) rings connected together [62]. Moreover, antidot arrays are ideal for investigating quantum coherence effects and phase coherence length of carriers. Antidot arrays impose lateral potential barriers that could create a bandgap in graphene [63], similar to the creation of the energy gap by introducing lateral periodic potentials from positive ion cores in a real semiconductor crystal. We have studied the magneto-transport properties of nanostructured antidot arrays in epitaxially grown graphene films on SiC ($000\bar{1}$). Pronounced AB oscillations, weak localization, and commensurability oscillations are observed, directly related to the electrical characteristics of epitaxial graphene films such as mean free path and phase coherence length.

The device structure of the fabricated graphene antidot array is shown in Fig. 6.13a, b. The graphene film for this particular experiment was grown at 1,600°C in vacuum for 10 min on C-face of SiC substrate. Device isolation and antidot formation of the graphene film is realized by O_2 plasma based dry etching with electron-beam-lithography (Vistec VB-6 UHR-EWF) defined HSQ resist as the protection layer. The diameter of the holes is around 40 nm and the defined antidot array period is 80 nm. Ti/Au metallization is used to form the two terminal Ohmic contacts on graphene film. Two-point resistance measurements are performed in a variable temperature (0.4 K to 70 K) ^{3}He cryostat in magnetic fields up to 18 T using low frequency lock-in techniques. The external magnetic field (B) is applied normally to the graphene plane.

Figure 6.13c shows the magneto-conductance $G(B)$ of graphene antidot arrays as a function of perpendicular magnetic field at 0.47 K. The trace is essentially symmetric, $G(B) = G(-B)$, which is the reciprocity relation mandatory for a two-terminal measurement of a stable device. There are three distinguishing features of the measured magneto-conductance. The first is the pronounced weak localization dip around zero magnetic field. The second is distinct conductance minima at ± 4 T and ± 8 T. We attribute these minima to the commensurability between the cyclotron orbits of carriers in certain magnetic fields and the period of artificial holes as illustrated in Fig. 6.13b. There are three distinct types of carriers involved in magneto-transport in antidot arrays: pinned orbits, drifting orbits, and scattering orbits [61]. Pinned orbits remain localized about their orbit centers as shown in Fig. 6.13b and cannot contribute to transport. Pinned orbits play a central role here since they remove a fraction of carriers from the transport process. The magneto-conductance shows minima when the carriers with pinned orbits are trapped in this antidot array. Using the commensurability relation $2R_c = 2\sqrt{\pi N_s}(\hbar/eB) = a$, the carrier density N_s is determined to be $\sim 7.5 \times 10^{12}/\text{cm}^2$ within the right range for graphene films grown on C-face SiC, where R_c is the

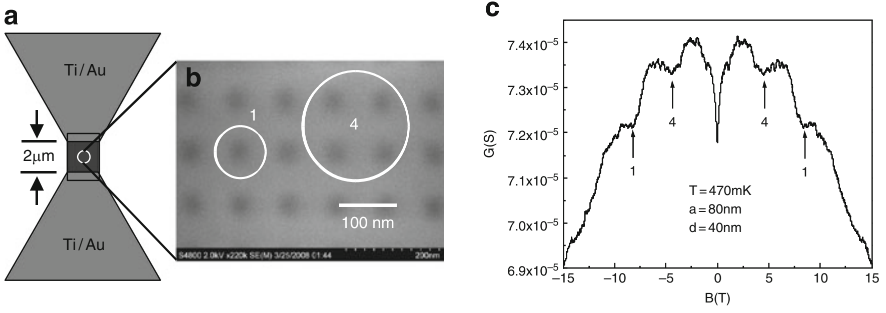

Fig. 6.13 (**a**) The sample layout with 2 μm×2 μm graphene area and two-terminal metal contacts. (**b**) Electron microscopic image of antidote arrays with ∼40 nm holes and ∼80 nm pitches. The commensurate orbits around 1 antidot and 4 antidots are sketched to illustrate the physical origin of Weiss oscillations. (**c**) Magneto-conductance of the graphene antidote arrays measured at $T =$ 477 mK. On top of the commensurability oscillations, periodic features are clearly visible as also highlighted in Fig. 6.14a

cyclotron radius, h is the Planck constant, and a is the period of antidot arrays. The elastic mean free path l_e is estimated to be about 220 nm in a reference sample without antidots. The elastic mean free path is $l_e = 2D/v_F$, where the carrier diffusive constant $D = E_F/2N_s e^2 \rho$, Fermi energy $E_F = \hbar v_F \sqrt{\pi N_s}$, and ρ is zero-field resistivity of graphene films [4]. The l_e is larger than the circumference of a single antidot (∼125 nm), but slightly smaller than the circumference of the central pinned orbits (∼250 nm). The conclusion from this estimate is that transport is not fully ballistic. The reason for the observation of the second magneto-conductance minima, corresponding to the pinned orbits around four antidots and requiring a much larger l_e, is not clear. Another possibility is magnetic focusing related phenomenon localized with the nanostructures of 40 nm dimension. The third feature is the tiny structures superimposed on the measured trace, for example, between ±2 T and ±7 T. Universal conductance fluctuations are suppressed since the sample size (∼2 μm) is much larger than the phase coherence length. A quantum interference effect is still observable because the antidot size (∼40 nm) is smaller than the phase coherence length. These tiny periodic features are identified as AB oscillations, which are related with each magnetic quantum flux penetrating in one antidot cell. AB oscillations on an exfoliated graphene film have been demonstrated experimentally on a single lithographically defined ring [64].

The black thick curve in Fig. 6.14a shows the measured magneto-conductance between +2 and +12 T with superimposed oscillatory features. By taking the difference of the measured curve and the black baseline curve obtained from smoothing the measured one, a pronounced AB periodically oscillatory curve is exhibited as shown as the grey curve in Fig. 6.14a. The AB oscillation period $\Delta B \approx 0.5$ T in this field range is consistent with the condition that the magnetic flux enclosed within the unit cell of the square antidot lattice changes by a single magnetic flux quantum, i.e., $\Delta B = (h/e)/a^2$ with $a = 80$ nm. The rms amplitude

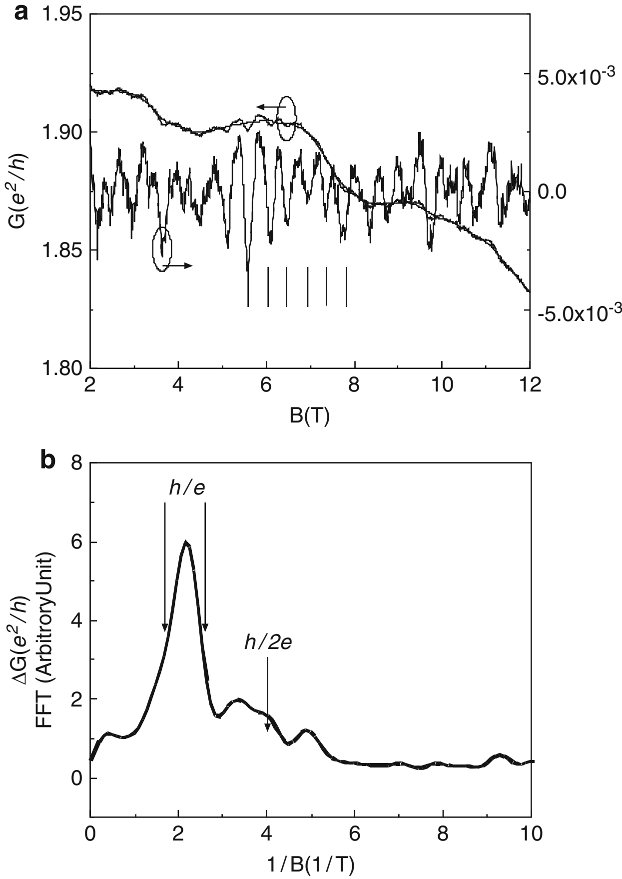

Fig. 6.14 (**a**) The *solid curve* is the measured magneto-conductance. The *thin curve* is the "baseline" after smoothing the original measured curve. The *periodically oscillatory curve* is the subtraction of the two black curves. *Vertical straight lines* are guided by eyes showing periodic B feature of observed AB oscillations. (**b**) Fourier spectrum of the oscillatory *grey curve* between 2 T and 12 T. The *solid curve* is after 6 points smoothing. The two *vertical straight lines* with *arrows* indicate the positions for half-height of the observed h/e peak, as used for the calculation of the inner and outer radii of AB-"ring" structure around one antidot

of AB oscillations is $\sim 0.01e^2/h$. For detailed discussions, Fig. 6.14b illustrates the Fourier power spectrum of Fig. 6.14a with a broad peak centered around 0.47 T, with 0.57 T and 0.40 T as the edge of the half-height width. It corresponds to the inner radius, middle radius, and outer radius of 48 nm, 53 nm, and 57 nm, respectively, if $\Delta B = (h/e)/(\pi r^2)$, where πr^2 is associated with the effective antidot area. It is consistent with the designed geometry well with 40 nm holes and 80 nm pitches. The relatively large inner radius could be related with overdeveloped resist patterns, plasma over-etching, and certain depletion length of graphene edges with

unpassivated dangling bonds. The magnetic length [$l_B = \sqrt{\hbar/eB} = 9.2\,\text{nm}$ at $B = 6\,\text{T}$] or similar edge channels in the quantum Hall regime could also affect the data. The observed AB oscillations demonstrate that the epitaxial graphene on SiC is of high-quality and at least has the quantum coherence length larger than 80–100 nm. The weak peak features around $1/B = 4(1/T)$ could be related to $h/2e$ oscillations [64].

While universal conductance fluctuations are generally observed in small graphene flakes, weak localization correction is strongly reduced compared to the conventional two-dimensional (2D) systems due to suppressed backscattering in graphene loosely coupled to the substrate [65–67]. Short range scattering in epitaxial graphene caused by tight binding to the substrate, short range scattering on the edges of antidots, and warping of the Fermi surface at high densities introduces intervalley scattering [68], which restores weak localization corrections [69]. We observe pronounced negative magneto-resistance at low fields with a sharp cusp at zero field characteristic of weak localization in 2D, as in Fig. 6.15a. Moreover, at higher fields magneto-resistance changes sign, which is expected for the case of strong

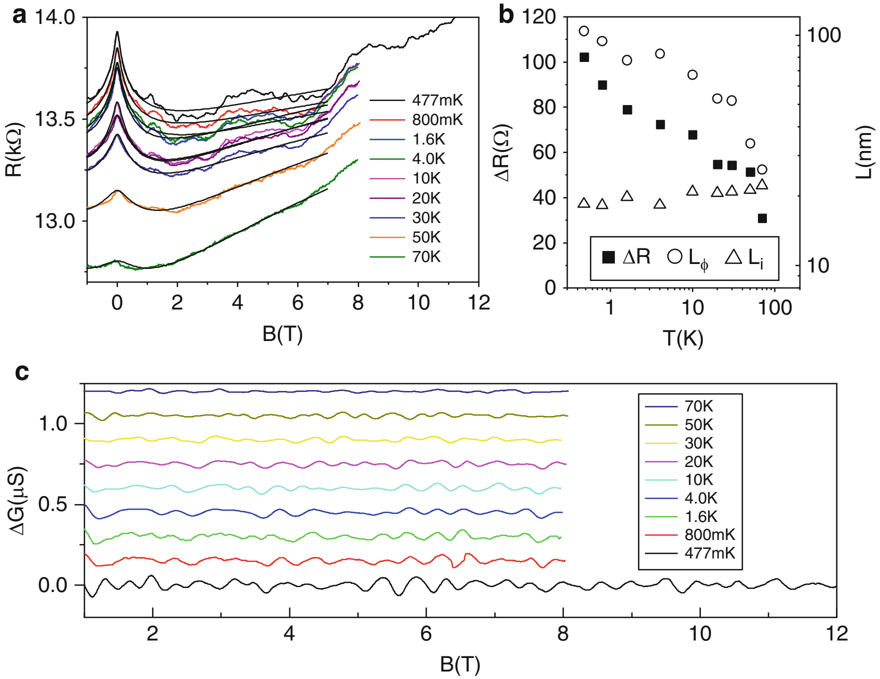

Fig. 6.15 (**a**) Magneto-resistance as a function of the sample temperature from 477 mK up to 70 K. The *solid black curves* are fitted weak localization curves in antidot arrays [70]. (**b**) The coherence length L_Φ and intervalley scattering length L_i of graphene film with antidot arrays versus sample temperatures. (**c**) Temperature dependence of AB oscillations. The traces are vertically shifted for clarity

intervalley scattering [70]. We used the theory developed in [70] to analyze the data and extract both the phase coherence length L_{Φ} and the intervalley scattering length L_{i}, shown in Fig. 6.15b. L_{i} is found to be temperature independent and is approximately equal to the distance between antidots, suggesting that scattering on the antidot edges is the dominant intervalley scattering mechanism in our samples. L_{Φ} decreases with the increasing temperature, although it does not follow $1/T$ dependence found in unpatterned graphene [68]. We note that the range of field, where weak localization is observed in antidot arrays is much larger than that for unpatterned samples. The temperature dependence of AB oscillations is also plotted in Fig. 6.15c, which is consistent with the data in Fig. 6.15b of weak localization peak fitting.

The intrinsically weak anti-localization of graphene and the restoring of weak localization by defects are of interest to further investigate and unveil the quality of epitaxial graphene. We have studied weak localization on unpatterned epitaxial graphene on SiC (0001). Figure 6.16b shows $\Delta\rho_{\mathrm{xx}} = \rho_{\mathrm{xx}}(B) - \rho_{\mathrm{xx}}(B = 0\,\mathrm{T})$ with $V_{\mathrm{g}} = 1.8\,\mathrm{V}$ at various temperatures for a sample grown at 1,600°C in a 10 mbar argon ambient. At the lowest temperature (e.g., 1.6 K), an overall negative magneto-resistance at low B is observed, typical of weak localization [71]. Although weak

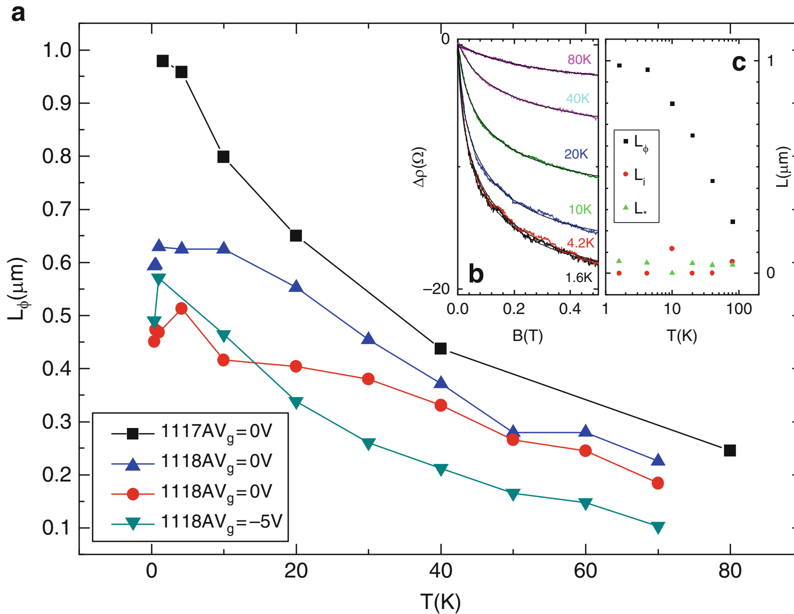

Fig. 6.16 Weak localization. (**a**) Phase coherent length for different devices. The corresponding electron densities are 2.0×10^{11} (bottom), 7.7×10^{11}, 1.0×10^{12}, and $2.4 \times 10^{12}/\mathrm{cm}^2$. (**b**) Magneto-resistance $\Delta\rho_{\mathrm{xx}} = \rho_{\mathrm{xx}}(B) - \rho_{\mathrm{xx}}(B = 0\,\mathrm{T})$ of sample 1,117 A for $V_{\mathrm{g}} = 1.8\,\mathrm{V}$ at various temperatures. The *colored curves* are experiment data, and the *black curves* are the fit. (c) Extracted characteristic lengths from the weak localization as a function of temperature for sample 1,117 A

localization in graphene is usually strongly reduced compared to the conventional 2D systems due to suppressed backscattering, strong intervalley scattering in epitaxial graphene tends to restore weak localization [69, 70, 72, 73]. We have fitted our experimental data using a theory developed by McCann et al. as before [70], and extracted the L_{Φ} (phase coherence length), L_{i} (intervalley scattering length), and L_{*} (intravalley scattering length) for each temperature as shown in Fig. 6.16c. Notice that all three lengths are much smaller than the sample size, indicating the edge is not the dominant scattering source, but rather disorder within the sample dominates scattering. L_{Φ} increases with decreasing temperature and reaches $\sim$1 μm at 1.6 K, while L_{i} and L_{*} are rather temperature insensitive. The extremely short L_{i} (a few nm) indicates a strong coupling of the single layer graphene to the SiC substrate, significantly different from the case studied in antidot case described in the above paragraphs or in [74], where the multi-layer graphene on the C-face SiC is relatively loosely coupled to the substrate, and the intervalley scattering arose mostly from the shape edges created by the antidot arrays. L_{*} here is about 40–50 nm, much larger than L_{i}, indicate moderate amount of other source of disorder larger than atomic scale. Similar analysis was also carried out for other devices grown at 1,600°C in vacuum. They show the similar temperature dependence and the extracted L_{Φ} are plotted against temperature for all devices as in Fig. 6.16a. They all decrease with the increase of the temperature, and decrease with decreasing carrier density across different samples, due to the effect of enhanced electron–electron interactions [72].

6.7 Spin Transport on Epitaxial Graphene

Spin transport in graphene has attracted intensive interest [75–78] in recent years for potential applications in spintronics due to its weak spin–orbit and hyperfine interactions [79]. In this session, we report on the first SpinFET (spin valve transistor) fabricated on an epitaxial graphene film grown on the C-face of a SiC substrate by high-temperature sublimation. Spin dependent magneto-resistance (MR) is observed from 400 mK to 3 K, showing a maximum spin signal of 0.25% and a maximum spin relaxation length of 200 nm at 400 mK. The multi-layer graphene film investigated here was formed on the C-face SiC at 1,550°C. AFM and SEM inspection confirms that it is possible to have a 2–10 μm domain size atomically smooth graphene films at that growth temperature as described in Sect. 6.2. Figure 6.17a shows the SEM image of one of the fabricated $Ni_{0.80}Fe_{0.20}$/Gr spin valve devices. All patterns were defined by electron-beam lithography. Ti/Au bonding pads were deposited on the graphene film, followed by an oxygen plasma dry etching to isolate the central graphene area with a width (W) of 2 μm and a length of 5 μm. Two $Ni_{0.80}Fe_{0.20}$ electrodes were evaporated for spin injection and detection. They are 400 nm and 1 μm wide, with a separation gap (L) of 400 nm.

Figure 6.17b presents a typical spin dependent MR measured at 400 mK. The magnetic field is applied parallel to the ferromagnetic electrodes and swept firstly from +0.5 T to −0.5 T and then from −0.5 T to +0.5 T. The MR curve exhibits a

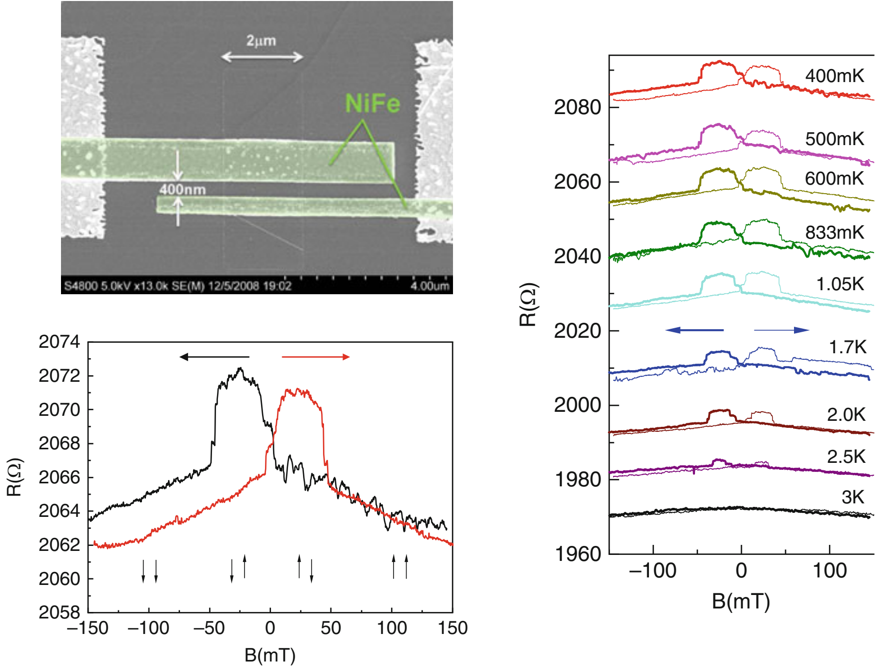

Fig. 6.17 (**a**) SEM image of a SpinFET fabricated on the epitaxial graphene film on SiC. (**b**) MR of the spin valve device measured at 400 mK. The magnetic field is aligned parallel to the ferromagnetic electrodes. The *small vertical arrows* show the magnetization of electrodes at different B fields. *Horizontal arrows* indicate the B field sweep polarity. (**c**) MR of the spin valve device measured at different temperatures from 400 mK to 3 K. The curves are shifted vertically for clarity

clear spin-valve hysteresis loop with a steep change at around ± 5 mT and ∓ 50 mT. The increase of MR is due to the magnetization reversal of the wider ferromagnetic electrode. The switch can occur before the zero-field condition due to multi-domains in the ferromagnetic electrodes, as discussed in [80].

A pronounced temperature dependence of the MR is observed in Fig. 6.17c. The curves are shifted vertically for clarity. As can be seen, both the magnitude and the width of the spin signals decrease as the temperature increases, and eventually disappears at 3 K. The spin relaxation length (λ_{sf}) can be estimated from the magnitude of the spin signals. The graphene sheet resistance (ρ) is estimated to be $\sim 1\,\mathrm{k}\Omega/\mathrm{sq}$ and $\sim 200\Omega$ in this device. However, the total resistance is $\sim 2\,\mathrm{k}\Omega$. The contact resistance is much larger than the spin resistance [81, 82]. The large contact-resistance suggests the $Ni_{0.80}Fe_{0.20}$/graphene junctions could be quasi-tunneling like. XPS studies of the $Ni_{0.80}Fe_{0.20}$/graphite interface indicates that C–O bonds are formed if $Ni_{0.80}Fe_{0.20}$ is deposited on a DI water exposed surface. Assuming that the interfacial C–O bonding leads to tunneling-like spin injection, the spin signal for a local measurement on 2D system can be described simply as,

$R_s = 2P^2\lambda_{sf}\rho e^{-L/\lambda sf}/W$, where the spin polarization P is 0.48 for $Ni_{0.80}Fe_{0.20}$ [81, 82]. The low-limit estimated λ_{sf} versus temperature is 200 nm at 0.4 K and 100 nm at 3 K. The reproducible step-like features are observed on up and down slopes of MR around ± 5 mT and ∓ 50 mT. These may be related with a sequence of mesoscopic domain switching in the ferromagnetic electrodes. The origin of the observed strong temperature-dependent spin effect in graphene is not fully understood. More work are needed on synthesis, process optimization, and physical understanding for an epitaxial graphene SpinFET operating at room temperature.

6.8 Summary

We have systematically studied graphene synthesis on SiC substrates by high-temperature sublimation in vacuum and argon ambient. Monolayer graphene on Si-face of SiC with a room-temperature mobility of 1,500–2,500 cm^2/Vs and multi-layer graphene on C-face of SiC with a mobility of 5,000–18,000 cm^2/Vs are obtained. A high-k gate stack on epitaxial graphene is realized by inserting a fully oxidized nanometer thin aluminum film as a seeding layer followed by an atomic-layer deposition process. The QHE and SdH in epitaxial graphene on SiC (0001) are systematically studied at different temperatures and different top gate bias. This quantum experiment confirms that epitaxial graphene on SiC shares the same relativistic physics as the exfoliated graphene, and the universal scaling in plateau to plateau transition also holds for epitaxial graphene films. Ballistic and coherent transport properties are studied through graphene antidot arrays with the pronounced AB oscillations. SpinFET is also demonstrated at low temperature on epitaxial graphene. All the work shows that epitaxial graphene on SiC provides a platform for future microelectronic and nanoelectronic applications beyond what exfoliated graphene can offer.

Acknowledgements The authors would like to thank the close collaborations with J.A. Cooper, Jr., R. Reifenberger, L.W. Engel, L.P. Rokhinson, E.A. Stach, R.M. Wallace, J. Appenzeller, J.J. Gu, Y. Xuan, M. Xu, K. Xu, and A.T. Neal. The authors also would like to thank G. Jones, T. Murphy, and E. Palm at National High Magnetic Field Laboratory (NHMFL) for experimental assistance. Part of the work on graphene is supported by NRI (Nanoelectronics Research Initiative) through MIND (Midwest Institute of Nano-electronics Discovery), DARPA, and Intel Cooperation. NHMFL is supported by NSF Grant Nos. DMR-0084173 and ECS-0348289, the State of Florida, and DOE.

References

1. A.K. Geim, K.S. Novoselov, Nat. Mater. **6**, 183 (2007)
2. K.S. Novoselov, A.K. Geim, S.V. Morozov, D. Jiang, Y. Zhang, S.V. Dubonos, I.V. Grigorieva, A.A. Firsov, Science **306**, 666 (2004)
3. Y. Zhang, Y.W. Tan, H.L. Stormer, P. Kim, Nature **438**, 201 (2005)

4. C. Berger, Z. Song, X. Li, X. Wu, N. Brown, C. Naud, D. Mayou, T. Li, J. Hass, A.N. Marchenkov, E.H. Conrad, P.N. First, W.A. de Heer, Science **312**, 1191 (2006)
5. Y.Q. Wu, P.D. Ye, M.A. Capano, Y. Xuan, Y. Sui, M. Qi, J.A. Cooper, T. Shen, D. Pandey, G. Prakash, R. Reifenberger, Appl. Phys. Lett. **92**, 092102 (2008)
6. G. Gu, S. Niu, R.M. Feenstra, R.P. Devaty, W.J. Choyke, W.K. Chan, M.G. Kane, Appl. Phys. Lett. **90**, 253507 (2007)
7. J. Kedzierski, P.L. Hsu, P. Healey, P.W. Wyatt, C.L. Keast, M. Springkle, C. Berger, W.A. de Heer, IEEE Trans. Electron Devices **55**, 2078 (2008)
8. J.S. Moon, D. Curtis, M. Hu, D. Wong, C. McGuire, P.M. Campbell, G. Jerigan, J. Tedesco, B. VanMil, R. Myers-Ward, C. Edy Jr., D.K. Gaskill, IEEE Electron Device Lett. **30**, 650 (2009)
9. Y.M. Lin, C. Dimitrakopoulos, K.A. Jenkins, D.B. Farmer, H.Y. Chiu, A. Gill, P. Avouris, Science **327**, 662 (2010)
10. K.S. Kim, Y. Zhao, H. Jang, S.Y. Lee, J.M. Kim, K.S. Kim, J.H. Ahn, P. Kim, J.Y. Choi, B.H. Hong, Nature **457**, 706 (2009)
11. A. Reina, X. Jia, J. Ho, D. Nezich, H. Son, V. Bulovic, M.S. Dresselhaus, J. Kong, Nano Lett. **9**, 30 (2009)
12. Q. Yu, J. Lian, S. Siriponglert, H. Li, Y.P. Chen, S.S. Pei, Appl. Phys. Lett. **93**, 113103 (2008)
13. X. Li, X. Cai, J. An, S. Kim, J. Nah, D. Yang, R. Piner, A. Velamakanni, I. Jung, E. Tutuc, S.K. Banerjee, L. Colombo, R.S. Ruoff, Science **324**, 1312 (2009)
14. A.J. Van Bommel, J.E. Crombeen, A. Van Tooren, Surf. Sci. **48**, 463 (1975)
15. C. Berger et al., J. Phys. Chem. B **108**, 19912 (2004)
16. M.Y. Han, B. Ozyilmaz, Y. Zhang, P. Kim, Phys. Rev. Lett. **98**, 206805 (2007)
17. Z. Chen, Y.M. Lin, M.J. Rooks, P. Avouris, Physica E **40**, 228 (2007)
18. D.V. Kosynkin et al., Nature **458**, 872 (2009)
19. X. Li, X. Wang, L. Zhang, S. Lee, H. Dai, Science **319**, 1229 (2008)
20. X. Wang et al., Phys. Rev. Lett. **100**, 206803 (2008)
21. L. Jiao, L. Zhang, X. Wang, G. Diankov, H. Dai, Nature **458**, 877 (2009)
22. J. Bai, X. Duan, Y. Huang, Nano Lett. **9**, 2083 (2009)
23. X. Wang, H. Dai, Nat. Chem. **2**, 661 (2010)
24. T. Ohta, A. Bostwick, T. Seyller, K. Horn, E. Rotenberg, Science **313**, 951 (2006)
25. E.V. Castro, K.S. Novoselov, S.V. Morozov, N.M.R. Peres, J.M.B. Lopes dos Santos, J. Nilsson, F. Guinea, A.K. Geim, A.H. Castro Neto, Phys. Rev. Lett. **99**, 216902 (2007)
26. J.B. Oostinga, H.B. Heersche, X. Liu, A.F. Morpurgo, L.M.K. Vandersypen, Nat. Mater. **7**, 151 (2008)
27. Y. Zhang, T.T. Tang, C. Girit, Z. Hao, M.C. Martin, A. Zettl, M.F. Crommie, Y.R. Shen, F. Wang, Nature **459**, 820 (2009)
28. F. Xia, D.B. Farmer, Y.M. Lin, P. Avouris, Nano Lett. **10**, 715 (2010)
29. Y. Xuan, Y. Wu, T. Shen, M. Qi, M.A. Capano, J.A. Cooper, P.D. Ye, Appl. Phys. Lett. **92**, 013101 (2008)
30. X. Wang, S.M. Tabakman, H. Dai, J. Am. Chem. Soc. **130**, 8152 (2008)
31. J.R. Williams, L. DiGarlo, C.M. Marcus, Science **317**, 638 (2007)
32. S. Kim, J. Nah, I. Jo, D. Shahrjerdi, L. Colombo, Z. Yao, E. Tutuc, S.K. Banerjee, Appl. Phys. Lett. **94**, 062107 (2008)
33. T. Shen, J.J. Gu, M. Xu, Y.Q. Wu, M.L. Bolen, M.A. Capano, L.W. Engel, P.D. Ye, Appl. Phys. Lett. **95**, 172105 (2009)
34. D.B. Farmer, H.Y. Chiu, Y.M. Lin, K.A. Jenkins, F. Xia, P. Avouris, Nano Lett. **9**, 4474 (2009)
35. Q.H. Wang, M.C. Hersam, Nat. Chem. **1**, 206 (2009)
36. B. Lee, S.Y. Park, H.C. Kim, K.J. Cho, E.M. Vogel, M.J. Kim, R.M. Wallace, J. Kim, Appl. Phys. Lett. **92**, 203102 (2008)
37. L.B. Biedermann, M.L. Bolen, M.A. Capano, D. Zemlyanov, R. Reifenberger, Phys. Rev. B**79**, 125411 (2009)
38. S.E. Harrison, M.A. Capano, R. Reifenberger, Appl. Phys. Lett. **96**, 081905 (2010)
39. M.L. Bolen, S.E. Harrison, L.B. Biedermann, M.A. Capano, Phys. Rev. B **80**, 121411 (2010)

40. M.L. Bolen, T. Shen, J.J. Gu, R. Colby, E.A. Stach, P.D. Ye, M.A. Capano, J. Electron. Mater. **39**, 2696 (2010)
41. J. Jobst, D. Waldmann, F. Speck, R. Hirner, D.K. Maude, T. Seyller, H.B. Weber, Phys. Rev. B **81**, 195434 (2010)
42. A. Tzalenchuk, S. Lara-Avila, A. Kalaboukhov, S. Paolillo, M. Syvajarvi, R. Yakimova, O. Kazalova, T.J.B.M. Janssen, V. Fal'ko, S. Kubatkin, Nat. Nanotechnol. **5**, 186 (2010)
43. X. Wu, Y. Hu, M. Ruan, N.K. Madiomanana, J. Hankinson, M. Sprinkle, C. Berger, W.A. de Heer, Appl. Phys. Lett. **95**, 223108 (2009)
44. J. Drowart, G. de Maria, G. Inghram, J. Chem. Phys. **29**, 1015 (1958)
45. S.G. Davis, D.F. Anthrop, A.W. Searcy, J. Chem. Phys. **34**, 659 (1961)
46. L. Muehlhoff, W.J. Choyke, M.J. Bozack, J.T. Yates, J. Appl. Phys. **60**, 2842 (1986)
47. J. Hass, F. Varchon, J.E. Millán-Otoya, M. Sprinkle, N. Sharma, W.A. de Heer, C. Berger, P.N. First, L. Magaud, E.H. Conrad, Phys. Rev. Lett. **100**, 125504 (2008)
48. J.L. Tedesco, B. VanMil, R.L. Myers-Ward, J. Culbertson, G. Jernigan, P. Campbell, J.M. McCrate, S.A. Kitt,, C. Eddy Jr., D.K. Gaskill, ECS Trans. **19**, 137 (2009)
49. K.V. Emtsev, A. Bostwick, K. Horn, J. Jobst, G.L. Kellogg, L. Ley, J.L. McChesney, T. Ohta, S.A. Reshanov, J. Röhrl, E. Rotenberg, A.K. Schmid, D. Waldmann, H.B. Weber, T. Seyller, Nat. Mater. **8**, 203 (2009)
50. J.L. Tedesco, B.L. VanMil, R.L. Myers-Ward, J.M. McCrate, S.A. Kitt, P.M. Campbell, G.G. Jernigan, J.C. Culbertson, J.C.R. Eddy, D.K. Gaskill, Appl. Phys. Lett. **95**, 122102 (2009)
51. D.B. Farmer, R.G. Gordon, Nano Lett. **6**, 699 (2006)
52. V. Barone, O. Hod, G.E. Scuseria, Nano Lett. **6**, 2748 (2006)
53. Y.W. Son, M.L. Cohen, S.G. Louie, Nature **444**, 347 (2006)
54. K. Xu, P.D. Ye, J. Phys. Chem. C **114**, 10505 (2010)
55. B. Huard, J.A. Sulpizio, N. Stander, K. Todd, B. Yang, D. Goldbaher-Gordon, Phys. Rev. Lett. **98**, 236903 (2007)
56. V.P. Gusynin S.G. Sharapov, Phys. Rev. B **71**, 125124 (2005)
57. H.P. Wei, D.C. Tsui, M.A. Paalanen, A.M.M. Pruisken, Phys. Rev. Lett. **61**, 1294 (1988)
58. W. Li, C.L. Vicente, J.S. Xia, W. Pan, D.C. Tsui, L.N. Pfeiffer, K.W. West, Phys. Rev. Lett. **102**, 216801 (2009)
59. S. Koch, R.J. Haug, K.v. Klitzing, K. Ploog, Phys. Rev. Lett. **67**, 883 (1991)
60. A.J.M. Giesbers, U. Zeitler, L.A. Ponomarenko, R. Yang, K.S. Novoselov, A.K. Geim, J.C. Maan, Phys. Rev. B **80**, 241411 (2009)
61. D. Weiss, M.L. Roukes, A. Menschig, P. Grambow, K. von Klitzing, G. Weimann, Phys. Rev. Lett. **66**, 2790 (1991)
62. D. Weiss, K. Richter, A. Menschig, R. Bergmann, H. Schweizer, K. von Klitzing, G. Weimann, Phys. Rev. Lett. **70**, 4118 (1993)
63. T.G. Pedersen, C. Flindt, J. Pedersen, N.A. Mortensen, A.P. Jauho, K. Pedersen, Phys. Rev. Lett. **100**, 136804 (2008)
64. S. Russo, J.B. Oostinga, D. Wehenkel, H.B. Heersche, S.S. Sobhani, L.M.K. Vandersypen, A.F. Morpurgo, Phys. Rev. B **77**, 85413 (2008)
65. T. Ando, T. Nakanishi, J. Phys. Soc. Jpn 67, 1704 (1998)
66. S.V. Morozov, K.S. Novoselov, M.I. Katsnelson, F. Schedin, L.A. Ponomarenko, D. Jiang, A.K. Geim, Phys. Rev. Lett. **97**, 016801 (2006)
67. H. Suzuura T. Ando Phys. Rev. Lett. **89**, 266603 (2002)
68. A.F. Morpurgo, F. Guinea, Phys. Rev. Lett. **97**, 196804 (2006)
69. F.V. Tikhonenko, D.W. Horsell, R.V. Gorbachev, A.K. Savchenko, Phys. Rev. Lett. **100**, 056802 (2008)
70. E. McCann, K. Kechedzhi, V.I. Fal'ko, H. Suzuura, T. Ando, B.L. Altshuler, Phys. Rev. Lett. **97**, 146805 (2006)
71. C.W.J. Beenakker, H. Vanhouten, Solid State Phys. **44**, 1 (1991)
72. D.K. Ki, D. Jeong, J.H. Choi, H.J. Lee, K.S. Park, Phys. Rev. B **78**, 125409 (2008)
73. X.S. Wu, X.B. Li, Z.M. Song, C. Berger, W.A. de Heer, Phys. Rev. Lett. **98**, 136801 (2007)

74. T. Shen, Y.Q. Wu, M.A. Capano, L.P. Rokhinson, L.W. Engel, P.D. Ye, Appl. Phys. Lett. **93**, 122102 (2008)
75. E.W. Hill, A.K. Geim, K. Novoselov, F. Schedin, P. Blake IEEE Trans. Magnet **42**, 2694–2696 (2006)
76. N. Tombros, C. Jozsa, M. Popinciuc, H.T. Jonkman B.J. van Wees Nature **448**, 571–U4 (2007)
77. H. Goto, A. Kanda, T. Sato, S. Tanaka, Y. ootuka, S. Odaka, H. Muyazaki, K. Tsukagoshi, Y. Aoyagi Appl. Phys. Lett. **92**, 212110 (2008)
78. M. Nishioka A.M. Goldman Appl. Phys. Lett. **90**, 252505 (2007)
79. D. Huertas Hernando, F. Guinea, A. Brataas Phys Rev. B **74**, 155426 (2006)
80. F.J. Jedema, M.S. Nijboer, A.T. Filip, B.J. van Wees Phys. Rev. B **67**, 085319 (2003)
81. C. Jozsa, M. Popinciuc, N. Tombros, H.T. Jonkman, B.J. van Wees Phys. Rev. B **79**, 081402 (R) (2009)
82. S. Takahashi S. Maekawa Phys. Rev. B **67**, 052409 (2003)